Eur. Phys. J. Plus (2020) 135:235
https://doi.org/10.1140/epjp/s13360-020-00216-y

THE EUROPEAN PHYSICAL JOURNAL PLUS

Regular Article

High-accuracy neutron diffusion calculations based on integral transport theory

Roy Gross[1], **Daniele Tomatis**[2], **Erez Gilad**[1,a]

[1] The Unit of Nuclear Engineering, Ben-Gurion University of the Negev, 8410501 Beersheba, Israel
[2] CEA, DEN, Service d'études des réacteurs et de mathématiques appliquées (SERMA), Université Paris-Saclay, 91191 Gif-sur-Yvette, France

Received: 20 May 2019 / Accepted: 8 January 2020

Abstract In this paper, the Ronen method is developed, implemented, and applied to resolve the neutron flux and the criticality eigenvalue in simple one-dimensional homogeneous and heterogeneous problems. The Ronen method is based on iterative calculations of correction factors to use in a multigroup diffusion model, where the factors are actually given by the integral transport equation. In particular, spatially dependent diffusion constants are modified locally in order to reproduce new estimates of the surface currents obtained by the integral transport operator. The diffusion solver employed in this study uses finite differences, and the transport-corrected currents are introduced into the numerical scheme as drift terms. The corrected solutions are compared against reference results from a discrete ordinate code. The results match well with the reference solutions, especially in the limit of fine meshes, but slow convergence of the scalar flux is reported.

1 Introduction

Neutron transport calculations on a full-core scale can be a highly intensive computational task. High-fidelity core design optimization or transient analyses can quickly become computationally impractical when using transport methods [1]. For example, about 10^{11} histories are needed in a full-core Monte Carlo calculation to achieve a 1% accuracy on local flux/power estimation [2]. Another problem is the huge number of variables and parameters to be stored and used during computation, e.g., tallies, geometry, cross sections, and depletion data. A conservative estimation of the memory needed for reasonably accurate full-core Monte Carlo neutronic calculation is in the range of terabytes (TBs) [2]. The growing demand for high-accuracy and high-precision full-core computations challenges not only today's high-end computing systems but will also challenge the near-future (e.g., Exascale) computers [1–3].

To overcome this difficulty, faster (and less accurate) multigroup neutron diffusion solvers are frequently used [4,5]. However, future Gen-IV reactor designs are characterized by strong heterogeneity in the core, e.g., axial and radial seed-blanket structures, as in the French ASTRID SFR CVF design [6], challenging the accuracy of diffusion calculations. Moreover, modern calculation schemes evolve toward so-called best-estimate codes, aiming at high accuracy [7].

[a] e-mail: gilade@bgu.ac.il

Published online: 10 February 2020

A crucial issue in obtaining an accurate diffusion calculation is the formulation of the diffusion coefficient [8,9]. The calculation of this parameter should be based on physical insights from the transport equation, such that the resulting diffusion approximation can really capture the transport phenomena of interest. Improved diffusion models obtained through transport corrections can be divided into two main classes. The first class is based on extending the P_1 model equations (and the associated boundary conditions) along with some closure scheme, such as the well-known SP_3 approximation [10]. The second class, to which this study belongs, is based on the re-calculation of correction factors within the multigroup diffusion framework [11].

In this paper, the development, implementation, and qualification of the Ronen method [12] in one-dimensional homogeneous and heterogeneous plane geometry are reported. This method is implemented as a highly accurate multigroup neutron diffusion solver based on novel transport corrections. The main hypothesis underlying the Ronen method is based on iterative calculations of the multigroup diffusion coefficients driven by the solutions of the integral transport equation [11,12].

The theoretical background is detailed in Sect. 2, the numerical implementation is described in Sect. 3, the results are presented in Sect. 4, and conclusions are brought in Sect. 5.

2 Theoretical background

2.1 The Ronen method

In 2004, Ronen [12] suggested to derive corrected diffusion coefficients using Fick's law and more accurate estimations of the neutron currents by means of integral transport operators, whereas the neutron flux is resolved by diffusion theory. Denoting the currents obtained by integral transport as "integral currents" $\boldsymbol{J}_{\mathrm{tr}}(\boldsymbol{r}, E)$ and the currents obtained by Fick's law as "diffusion currents" $\boldsymbol{J}_D(\boldsymbol{r}, E)$, the Ronen idea is based on changing the diffusion coefficient such that

$$\boldsymbol{J}_D(\boldsymbol{r}, E) = -D(\boldsymbol{r}, E)\nabla\phi(\boldsymbol{r}, E) = \boldsymbol{J}_{\mathrm{tr}}(\boldsymbol{r}, E). \tag{1}$$

Since these accurate estimates of the currents are based on a known flux distribution, it was also suggested to execute new diffusion calculations, thus updating iteratively the diffusion coefficients in the global calculation.

$$D^{(k+1)}(\boldsymbol{r}, E) = -\frac{|\boldsymbol{J}_{\mathrm{tr}}^{(k)}(\boldsymbol{r}, E)|}{|\nabla\phi^{(k)}(\boldsymbol{r}, E)|}, \tag{2}$$

where k is the iteration index. The use of a tensor notation is needed for the diffusion coefficient in general multidimensional problems.

The motivation for this method was to overcome the inherent limitation of Fick's law requiring smooth flux gradients and thus small neutron absorption rate with respect to scattering in general. Nevertheless, isotropic scattering remained as a basic postulate. For example, in a homogeneous slab with void boundary conditions, Eq. (2) takes the following form [12]

$$D^{(k+1)}(x, E) = -\frac{\frac{1}{2}\int_0^a \mathrm{d}x' E_2[\sigma(E)|x - x'|]\,\mathrm{Sgn}(x - x')q^{(k)}(x', E)}{\partial\phi^{(k)}(x, E)/\partial x}. \tag{3}$$

This idea was later used by Tomatis and Dall'Osso [11], who provided a numerical demonstration in a simple slab problem. Instead of updating the diffusion coefficient by the ratio

of the current and the flux gradient, as in Fick's law, they adopted the coarse mesh finite difference method (CMFD) for taking into account in the diffusion solver the new currents estimated by the integral transport operator. This technique, largely adopted in the literature of nodal methods [4,13], can avoid indeterminate divisions in case of vanishing flux gradients. They tested this implementation in a homogeneous bare slab using two-group cross sections representative of a realistic PWR assembly. It was observed that the Ronen method (RM) could drive the flux distribution away from diffusion and closer to the reference solution of the integral Boltzmann transport equation, regardless of the initial formulation used for the diffusion coefficient. As expected, the largest errors were located near the boundary where the transport effects are more pronounced, but slowly decreasing even after many iterations.

2.2 The one-dimensional Peierls equation

There are several ways to derive the integral expression for the flux in slab geometry. Most of them start with assuming homogeneous and isotropic scattering and sources, yielding the *Peierls equation* [8,14–18]. The derivation of expression for slab geometry (of thickness a) is straightforward, yielding

$$\begin{aligned}\phi(x,E) &= \frac{1}{2}\int_0^a \mathrm{d}x' E_1\left[\sigma(E)|x-x'|\right] Q(x',E), \text{ with}\\ Q(x,E) &= \int_0^\infty \mathrm{d}E'\sigma_s(E\leftarrow E')\phi(x,E') + S(x,E)\end{aligned} \tag{4}$$

and $E_1(x)$ as first-order exponential integral [19]. Note that this expression does not include the contribution of uncollided neutrons originated from an incoming angular flux at the boundaries.

The starting point for the derivation of the integral expression for the flux in slab geometry is to directly integrate along a line the transport equation [14,16–18]

$$\psi(\boldsymbol{r},\hat{\boldsymbol{\Omega}}) = \int_0^R \mathrm{d}R' Q(\boldsymbol{r}-R'\hat{\boldsymbol{\Omega}},\hat{\boldsymbol{\Omega}})\mathrm{e}^{-\tau(\boldsymbol{r},\boldsymbol{r}-R'\hat{\boldsymbol{\Omega}})} + \psi(\boldsymbol{r}-R\hat{\boldsymbol{\Omega}},\hat{\boldsymbol{\Omega}})\mathrm{e}^{-\tau(\boldsymbol{r},\boldsymbol{r}-R\hat{\boldsymbol{\Omega}})}, \tag{5}$$

where $\tau(\boldsymbol{r},\boldsymbol{r}-R'\hat{\boldsymbol{\Omega}})$ is the *optical length*, defined as

$$\tau(\boldsymbol{r},\boldsymbol{r}-R'\hat{\boldsymbol{\Omega}}) \equiv \int_0^{R'} \sigma(\boldsymbol{r}-R''\hat{\boldsymbol{\Omega}})\mathrm{d}R'. \tag{6}$$

Assuming isotropic scattering and homogeneous medium in one-dimension for Eq. (5) recovers Eq. (4).

In what follows, a generalization of Eq. (4) is derived for heterogeneous medium with anisotropic scattering.

2.3 Integral expressions for the neutron flux and current

Consider an infinite slab of width a. The angular flux in the slab is given by [18]

$$\psi(x,E,\mu) = \psi(0,E,\mu)\mathrm{e}^{-\tau(0,x,E)/\mu} + \int_0^x \mathrm{d}x' \frac{Q(x',E,\mu)}{\mu}\mathrm{e}^{-\tau(x',x,E)/\mu}, \qquad \mu>0, \tag{7a}$$

$$\psi(x,E,\mu) = \psi(a,E,\mu)\mathrm{e}^{\tau(x,a,E)/\mu} - \int_x^a \mathrm{d}x' \frac{Q(x',E,\mu)}{\mu}\mathrm{e}^{\tau(x,x',E)/\mu}, \qquad \mu<0, \tag{7b}$$

where

$$\tau(x', x, E) \equiv \mathrm{Sgn}(x - x') \int_{x'}^{x} \sigma(x'', E)\mathrm{d}x'' \tag{8}$$

and $Q(x, E, \mu)$ denotes total emission.

Only scattering in isotropic media is considered here: $\sigma_s(*, \hat{\boldsymbol{\Omega}}' \rightarrow \hat{\boldsymbol{\Omega}}) = \sigma_s(*, \mu_0)/2\pi$ with the angle cosine $\mu_0 = \hat{\boldsymbol{\Omega}}' \cdot \hat{\boldsymbol{\Omega}}$. The source terms are written by moments of Legendre polynomials after the usual expansion of the scattering cross sections in Legendre polynomials of μ_0, followed by the application of the addition theorem and by integration on spherical harmonics using the symmetries and rotational invariance of the slab geometry [8]. The cross sections of the source term are grouped for simplicity by introducing the l-th moments of the production cross section [11]

$$\sigma_l(x, E \leftarrow E') = \sigma_{s,l}(x, E \leftarrow E') + \delta_{l0}\frac{\chi(E)}{k_{\mathrm{eff}}}\nu\sigma_f(x, E'), \tag{9}$$

with the Legendre moments of the scattering cross section

$$\sigma_{s,l}(x, E \leftarrow E') = \int_{-1}^{1} \mathrm{d}\mu_0 P_l(\mu_0)\sigma_s(x, E \leftarrow E', \mu_0). \tag{10}$$

δ_{l0} in Eq. (9) is the Kronecker function equal to 1 only for $l = 0$ and zero otherwise. The multiplication factor k_{eff} applies here on the fission production since external sources are missing. The source term is then rewritten as

$$\begin{aligned} Q(x, E, \mu) &= \sum_{l=0}^{\infty} \frac{2l+1}{2} \int_0^{\infty} \mathrm{d}E' \sigma_{s,l}(x, E \leftarrow E')\psi_l(x, E')P_l(\mu) \\ &\quad + \frac{\chi(E)}{2k_{\mathrm{eff}}} \int_0^{\infty} \mathrm{d}E' \nu\sigma_f(x, E')\psi_0(x, E') \\ &= \sum_{l=0}^{\infty} \frac{2l+1}{2} \int_0^{\infty} \mathrm{d}E' \sigma_l(x, E \leftarrow E')\psi_l(x, E')P_l(\mu) \\ &= \sum_{l=0}^{\infty} \frac{2l+1}{2} \int_0^{\infty} \mathrm{d}E' q_l(x, E \leftarrow E')P_l(\mu) \\ &= \sum_{l=0}^{\infty} \frac{2l+1}{2} q_l(x, E)P_l(\mu), \end{aligned} \tag{11}$$

where the source angular moments are defined as

$$q_l(x, E) \equiv \int_0^{\infty} \mathrm{d}E' q_l(x, E \leftarrow E') \equiv \int_0^{\infty} \mathrm{d}E' \sigma_l(x, E \leftarrow E')\psi_l(x, E')\mathrm{d}E'. \tag{12}$$

Finally, we also expand the angular dependence of the uncollided boundary flux in a series of orthogonal Legendre polynomials:

$$\psi(x, E, \mu) = \sum_{l=0}^{\infty} \frac{2l+1}{2} P_l(\mu)\psi_l(x, E). \tag{13}$$

This allows dealing only with flux moments at the right hand side of Eq. (9).

The scalar flux ϕ^+ at x resulting from neutrons coming from the left, i.e., $x' < x$ ($\mu > 0$), is determined by substituting Eq. (13) in Eq. (7a) and integrating over the angle

$$\begin{aligned}\phi^+(x,E) &\equiv \int_0^1 \mathrm{d}\mu\,\psi(x,E,\mu)\\ &= \sum_{l=0}^{\infty}\frac{2l+1}{2}\left\{\psi_l(0,E)\int_0^1 \mathrm{d}\mu\,P_l(\mu)\mathrm{e}^{-\tau(0,x,E)/\mu}\right.\\ &\quad\left.+\int_0^x \mathrm{d}x' q_l(x',E)\int_0^1 \mathrm{d}\mu\frac{P_l(\mu)}{\mu}\mathrm{e}^{-\tau(x',x,E)/\mu}\right\}. \end{aligned} \tag{14}$$

In order to solve the angular integrals, we resort to the following result [20,21]

$$\int_0^1 \mu^i P_l(\mu)\mathrm{e}^{-y/\mu}\mathrm{d}\mu = \sum_{m=0}^{[l/2]} h_m E_{l+2+i-2m}(y), \tag{15}$$

where the coefficients h_m are used to rewrite the Legendre polynomials as simple sums of weighted monomials, like

$$P_l(x)=\sum_{m=0}^{[l/2]} h_m x^{l-2m},\quad h_m = \frac{(-1)^m(2l-2m)!}{2^l m!(l-m)!(l-2m)!}\quad\text{and}\quad [l/2]=\begin{cases} l/2, & l \text{ even},\\ (l-1)/2, & l \text{ odd}.\end{cases} \tag{16}$$

Hence, the contribution to the flux from $x' < x$ can be written as

$$\begin{aligned}\phi^+(x) &= \sum_{l=0}^{\infty}\frac{2l+1}{2}\sum_{m=0}^{[l/2]} h_m\left\{E_{l+2-2m}[\tau(0,x,E)]\psi_l(0,E)\right.\\ &\quad\left.+\int_0^x \mathrm{d}x' E_{l+1-2m}[\tau(x',x,E)]q_l(x',E)\right\}. \end{aligned} \tag{17}$$

The contribution to the flux from $x' > x$ ($\mu < 0$) can be calculated in a similar manner, using the change of variables $\eta = -\mu$ for the angular integrals and the fact that $P_l(-\mu) = (-1)^l P_l(\mu)$. Hence, the expression for the scalar flux which accounts for anisotropic scattering and heterogeneous medium is

$$\begin{aligned}\phi(x,E) &= \phi^+(x,E)+\phi^-(x,E)\\ &= \sum_{l=0}^{\infty}\frac{2l+1}{2}\sum_{m=0}^{[l/2]} h_m\left\{E_{l+2-2m}[\tau(0,x,E)]\psi_l(0,E)\right.\\ &\quad+(-1)^l E_{l+2-2m}[\tau(x,a,E)]\psi_l(a,E)+\int_0^x \mathrm{d}x' E_{l+1-2m}[\tau(x',x,E)]q_l(x',E)\\ &\quad\left.+(-1)^l\int_x^a \mathrm{d}x' E_{l+1-2m}[\tau(x,x',E)]q_l(x',E)\right\}. \end{aligned} \tag{18}$$

The generalization of Eq. (18) to current is obtained in a similar procedure according to

$$\begin{aligned}J(x,E) &= J^+(x,E)-J^-(x,E) = \int_0^1 \mathrm{d}\mu\mu\psi(x,E,\mu)-\int_0^{-1}\mathrm{d}\mu\mu\psi(x,E,\mu)\\ &= \sum_{l=0}^{\infty}\frac{2l+1}{2}\sum_{m=0}^{[l/2]} h_m\left\{E_{l+3-2m}[\tau(0,x,E)]\psi_l(0,E)\right. \end{aligned}$$

$$+ (-1)^{l+1} E_{l+3-2m}[\tau(x, a, E)]\psi_l(a, E)$$
$$+ \int_0^x \mathrm{d}x' E_{l+2-2m}[\tau(x', x, E)]q_l(x', E)$$
$$+ (-1)^{l+1} \int_x^a \mathrm{d}x' E_{l+2-2m}[\tau(x, x', E)]q_l(x', E)\Big\}. \tag{19}$$

3 Numerical implementation

The cross sections, as well as the diffusion coefficient, are usually available as volume-averaged data per cell in the mesh. Once the scalar flux is known from the finite differences solver using the original diffusion coefficients, the integral expressions derived in Sect. 2.3 can be used to get new estimates of the currents J at the cell interfaces.

Instead of computing new diffusion coefficients at the interfaces by Fick's law, $J_\mathrm{D}(x, E) = -D(E)\partial_x\phi(x, E)$, new corrective currents $\delta J(x_s, E) = J_\mathrm{tr}(x_s, E) - J_\mathrm{D}(x_s, E)$ are obtained at cell interfaces x_s. Here, $J_\mathrm{D}(x, E)$ is called the "diffusion current" and is obtained using Fick's law, with the original values of the diffusion coefficients and with the derivative approximated by finite differences. In one-dimensional geometry and using the notation in Fig. 1, the diffusion current is evaluated according to

$$J_\mathrm{D}(x_{i+1/2}, E) \cong -D(x_{i+1/2}, E)\frac{\phi(x_{i+1}, E) - \phi(x_i, E)}{(\Delta x_{i+1} + \Delta x_i)/2}, \tag{20}$$

and the corrective current is defined according to

$$\delta J(x_{i+1/2}, E) = -\delta D(x_{i+1/2}, E)\frac{\phi(x_{i+1}, E) + \phi(x_i, E)}{(\Delta x_{i+1} + \Delta x_i)/2}, \tag{21}$$

where integer and rational subscripts indicate node-averaged and interface quantities, respectively. It is Eq. (21) from which the correction factors δD are obtained. The discretized form of the current δJ must involve the neighboring flux as well, but its representation is changed into a drift-advection term to get rid of possible undefined division by zeros in case of flat flux [11,13]. The so-called transport current $J_\mathrm{tr}(x_s, E)$ is evaluated using the integral expression derived in Sect. 2.3 as described in Sect. 3.2.

The input diffusion coefficients are provided as cell averaged quantities, but they are always needed at interfaces. Therefore, they are approximated here by local volume averages:

$$D(x_{i+1/2}, E) = \frac{\Delta x_i D(x_i, E) + \Delta x_{i+1} D(x_{i+1}, E)}{\Delta x_i + \Delta x_{i+1}}. \tag{22}$$

3.1 The correction as a drift term

The new numerical corrections δD are obtained at the interfaces using Eq. (21) to be used in the finite differences solver, together with the diffusive currents from Eq. (20). Hence, the neutron balance resolved by the CMFD takes into account both types of currents J_D and δJ.

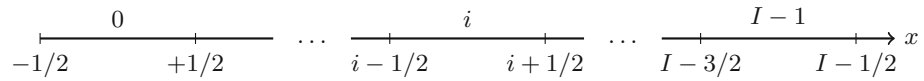

Fig. 1 Notation of the one-dimensional mesh

In particular, the one-dimensional multigroup neutron balance CMFD diffusion equations actually solved are

$$J^{+}_{D,g}(x) + \delta J^{+}_{g}(x) - J^{-}_{D,g}(x) - \delta J^{-}_{g}(x) + \sigma_g \phi_g(x) = \frac{\chi_g}{k_{\text{eff}}} \sum_{g'=1}^{G} \nu\sigma_{f,g'}(x)\phi_{g'}(x) + \sum_{g'=1}^{G} \sigma_{s,g\leftarrow g'}\phi_{g'}(x), \quad (23)$$

where $J^{\pm}_{D,g}(x) \equiv J_{D,g}(x_{i\pm 1/2})$.

Using the definitions in Eqs. (20)–(22) with the notation shown in Fig. 1, the discretized form of Eq. (23) is

$$-2D^{g}_{i+1/2}\frac{\phi_{i+1,g}-\phi_{i,g}}{\Delta x_{i+1}+\Delta x_i} - 2\delta D^{g}_{i+1/2}\frac{\phi_{i+1,g}+\phi_{i,g}}{(\Delta x_{i+1}+\Delta x_i)} + 2D^{g}_{i-1/2}\frac{\phi_{i,g}-\phi_{i-1,g}}{\Delta x_i+\Delta x_{i-1}} + 2\delta D^{g}_{i-1/2}\frac{\phi_{i,g}+\phi_{i-1,g}}{(\Delta x_i+\Delta x_{i-1})} + \sigma^{g}_{i}\phi_{i,g} = \sum_{g'=1}^{G}\sigma^{g\leftarrow g'}_{s,i}\phi_{i,g'} + \frac{\chi_g}{k_{\text{eff}}}\sum_{g'=1}^{G}\nu\sigma^{g'}_{f,i}\phi_{i,g'}. \quad (24)$$

Rearranging terms, one gets

$$\left(\frac{-D^{g}_{i-1/2}+\delta D^{g}_{i-1/2}}{\Delta x_{i-1}+\Delta x_i}\right)\phi_{i-1,g} + \left[\frac{D^{g}_{i+1/2}-\delta D^{g}_{i+1/2}}{\Delta x_{i+1}+\Delta x_i} + \frac{D^{g}_{i-1/2}+\delta D^{g}_{i-1/2}}{\Delta x_i+\Delta x_{i-1}} + \frac{\sigma^{g}_{i}}{2}\right]\phi_{i,g} + \left(\frac{-D^{g}_{i+1/2}-\delta D^{g}_{i+1/2}}{\Delta x_{i+1}+\Delta x_i}\right)\phi_{i+1,g} = \frac{1}{2}q_{i,g}, \quad (25)$$

where $q_{i,g}$ is the RHS of Eq. (24).

These equations can be formulated in operators notation according to

$$\mathcal{A}\Phi = \frac{1}{k_{\text{eff}}}\mathcal{F}\Phi, \quad (26)$$

where $\mathcal{A}$ is the migration operator, whose entries are given by Eq. (25) making it a three-diagonal banded matrix, and $\mathcal{F}$ is the neutron generation operator given by the second term in $q_{i,g}$ (see Eqs. 24–25). Note that $\mathcal{A}$ can be written as $\mathcal{A} = \mathcal{A}_0 + \delta\mathcal{A}$ distinguishing the diffusion corrections from the constant diffusion coefficients derived from the transport problem. In the homogeneous case, $\mathcal{A}(x) = \mathcal{A}_0 + \delta\mathcal{A}(x)$.

3.2 Evaluation of the currents by the integral form of the transport equation

The numerical evaluation of the neutron current $J_g(x)$ at the cell interfaces requires spatial integration of Eq. (19). The neutron current at any interface can be calculated by considering separately contributions from all cells which are to the left or to the right of the interface itself. The current at a cell interface is discretized as follows

$$J_g(x_{i+1/2}) = \sum_{l=0}^{\infty}\frac{2l+1}{2}\sum_{m=0}^{[l/2]}h_m\Big\{E_{n_{l,m}+1}[\tau_g(0,x_{i+1/2})]\psi_{l,g}(0) + (-1)^{l+1}E_{n_{l,m}+1}[\tau_g(x_{i+1/2},a)]\psi_{l,g}(a)$$

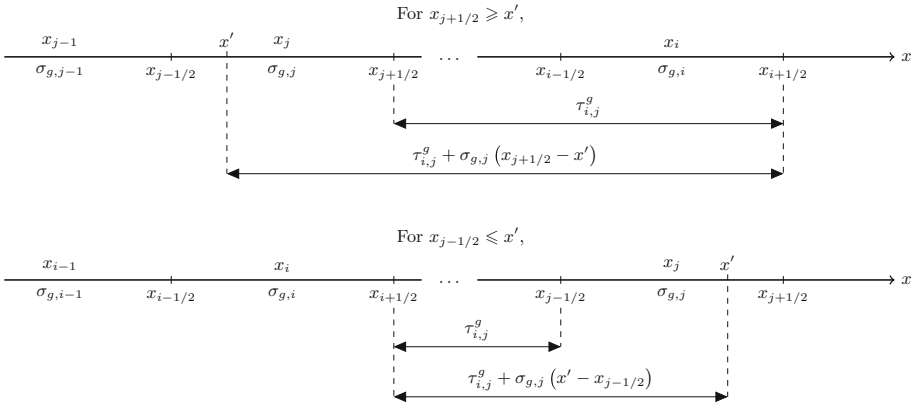

Fig. 2 Notation for numerical evaluation of interface currents by the integral form of the transport equation

$$+\sum_{j=0}^{i} q_{l,g,j} \int_{x_{j-1/2}}^{x_{j+1/2}} \mathrm{d}x' E_{n_{l,m}}[\tau_g(x', x_{i+1/2})]$$
$$+ (-1)^{l+1} \sum_{j=i+1}^{I-1} q_{l,g,j} \int_{x_{j-1/2}}^{x_{j+1/2}} \mathrm{d}x' E_{n_{l,m}}[\tau_g(x_{i+1/2}, x')]\Bigg\}, \tag{27}$$

where $n_{l,m} \equiv l + 2 - 2m$. The source $q_{l,g,j}$ is the l^{th} angular moment of the volume-average within-group source in the cell j. The optical lengths show the subscript g because they are evaluated with the corresponding total cross section σ_g. Note that for void boundary conditions, the boundary terms must vanish by definition. The spatial integrals in Eq. (27) can be solved analytically knowing that $E'_{n+1}(u) = -E_n(u)$ [22]. The optical length between the right surfaces of cell j and cell i is

$$\tau^g_{i,j} \equiv \begin{cases} \sum_{k=j+1}^{i} \sigma_{g,k} \Delta x_k & \text{if } i > j, \\ 0 & \text{if } i = j, \\ \sum_{k=i+1}^{j} \sigma_{g,k} \Delta x_k & \text{if } i < j. \end{cases} \tag{28}$$

The general case follows in Fig. 2.

After substitution, the integration of the $E_{n_{l,m}}$ terms in Eq. (27) yields

$$\begin{aligned} \int_{x_{j-1/2}}^{x_{j+1/2}} \mathrm{d}x' E_{n_{l,m}}[\tau_g(x', x_{i+1/2})] &= \frac{1}{\sigma_{g,j}} \left[E_{n_{l,m}+1}(\tau^g_{i \geqslant j}) - E_{n_{l,m}+1}(\tau^g_{i \geqslant j} + \sigma_{g,j} \Delta x_j) \right] \\ &= \frac{1}{\sigma_{g,j}} \left\{ E_{n_{l,m}+1}\left[\tau_g(x_{j+1/2}, x_{i+1/2})\right] \right. \\ &\quad \left. - E_{n_{l,m}+1}\left[\tau_g(x_{j-1/2}, x_{i+1/2})\right] \right\}, \end{aligned} \tag{29a}$$

$$\int_{x_{j-1/2}}^{x_{j+1/2}} \mathrm{d}x' E_{n_{l,m}}[\tau_g(x_{i+1/2}, x')] = \frac{1}{\sigma_{g,j}} \left[E_{n_{l,m}+1}(\tau^g_{i<j}) - E_{n_{l,m}+1}(\tau^g_{i<j} + \sigma_{g,j}\Delta x_j) \right]$$
$$= \frac{1}{\sigma_{g,j}} \left\{ E_{n_{l,m}+1}\left[\tau_g(x_{i+1/2}, x_{j-1/2})\right] - E_{n_{l,m}+1}\left[\tau_g(x_{i+1/2}, x_{j+1/2})\right] \right\}. \quad (29b)$$

Hence, the interface currents can be written as

$$J_g(x_{i+1/2}) = \sum_{l=0}^{\infty} \frac{2l+1}{2} \sum_{m=0}^{[l/2]} h_m \Bigg\{ E_{n_{l,m}+1}[\tau_g(0, x_{i+1/2})]\psi_{l,g}(0)$$
$$+ (-1)^{l+1} E_{n_{l,m}+1}[\tau_g(x_{i+1/2}, a)]\psi_{l,g}(a)$$
$$+ \sum_{j=0}^{i} \frac{q_{l,g,j}}{\sigma_{g,j}} \left\{ E_{n_{l,m}+1}\left[\tau_g(x_{j+1/2}, x_{i+1/2})\right] - E_{n_{l,m}+1}\left[\tau_g(x_{j-1/2}, x_{i+1/2})\right] \right\}$$
$$+ (-1)^{l+1} \sum_{j=i+1}^{I-1} \frac{q_{l,g,j}}{\sigma_{g,j}} \left\{ E_{n_{l,m}+1}\left[\tau_g(x_{i+1/2}, x_{j-1/2})\right] \right.$$
$$\left. - E_{n_{l,m}+1}\left[\tau_g(x_{i+1/2}, x_{j+1/2})\right] \right\} \Bigg\}. \quad (30)$$

Note that for the isotropic case ($l = 0$) Eq. (30) reduces to

$$J_g(x_{i+1/2}) = \frac{1}{2} \Bigg\{ E_3[\tau_g(0, x_{i+1/2})]\psi_{0,g}(0) - E_3[\tau_g(x_{i+1/2}, a)]\psi_{0,g}(a)$$
$$+ \sum_{j=0}^{i} \frac{q_{0,g,j}}{\sigma_{g,j}} \left\{ E_3\left[\tau_g(x_{j+1/2}, x_{i+1/2})\right] - E_3\left[\tau_g(x_{j-1/2}, x_{i+1/2})\right] \right\}$$
$$- \sum_{j=i+1}^{I-1} \frac{q_{0,g,j}}{\sigma_{g,j}} \left\{ E_3\left[\tau_g(x_{i+1/2}, x_{j-1/2})\right] - E_3\left[\tau_g(x_{i+1/2}, x_{j+1/2})\right] \right\} \Bigg\}$$
$$= \frac{1}{2} \Bigg\{ E_3[\tau_g(0, x_{i+1/2})]\psi_{0,g}(0) - E_3[\tau_g(x_{i+1/2}, a)]\psi_{0,g}(a)$$
$$+ \sum_{j=0}^{I-1} \frac{q_{0,g,j}}{\sigma_{g,j}} \left\{ E_3\left[\tau_g(x_{j+1/2}, x_{i+1/2})\right] - E_3\left[\tau_g(x_{j-1/2}, x_{i+1/2})\right] \right\} \mathrm{Sgn}(i-j) \Bigg\}. \quad (31)$$

It is possible to identify in these equations transfer probabilities of neutrons emitted by the sources $q_{l,g,j}$ and crossing the right interface of cell i without colliding. The quantities $E_{n_{l,m}}[\tau_g(x_i, x_j)]$ allowing to compute these probabilities can be pre-calculated once and stored in multidimensional arrays for later use.

3.3 Boundary conditions

A generalized form for the boundary condition (at the left) follows as

$$J_{\mathrm{D}}(x = 0) = -D_0 \frac{\phi_0}{\Delta x_0/2 + \zeta}, \quad (32)$$

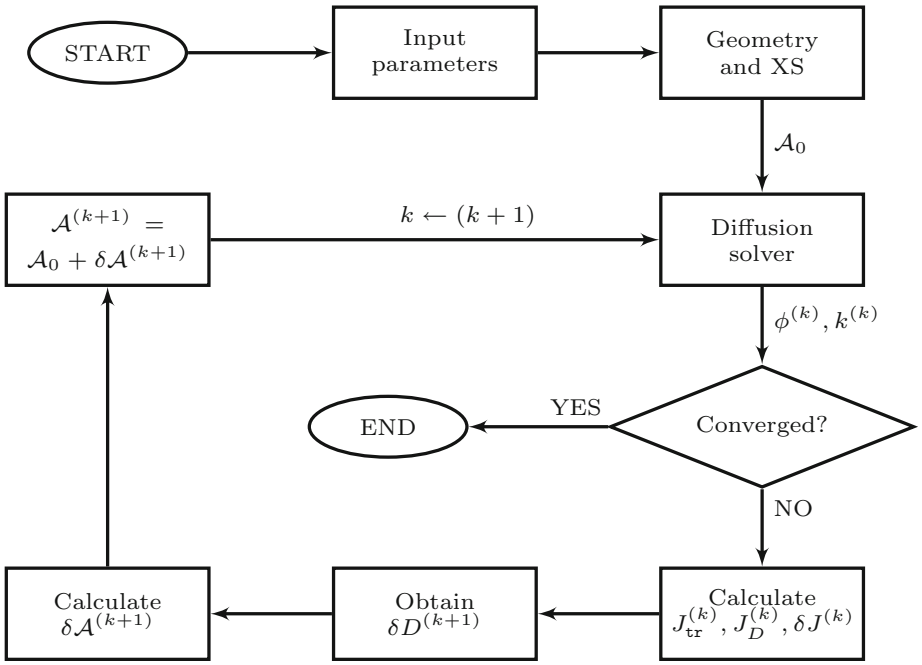

Fig. 3 A flowchart of the Ronen algorithm

where ζ is the extrapolation length in case of vacuum. The Marshak boundary conditions are reproduced by $\zeta = 2D$, but the more accurate value $\zeta \approx 2.13D$ is taken to match transport with better agreement [23]. Reflection can be reproduced by $\zeta \to \infty$, whereas the condition of zero-flux is realized by $\zeta = 0$. The quantity δJ at the boundary takes the simpler form of $\delta J = -\delta D_{-1/2}\phi_0$, without dividing by the spatial width, since no particular extrapolation length is appropriate for the correction. The expression for the right boundary is straightforward, implying a nonnegative current. One should recall that the diffusion coefficient remains constant throughout the calculation and so is the extrapolated distance. Only δD is recalculated and the correction is actually implemented through the currents, i.e., $J_{\mathrm{tr}} = J_{\mathrm{D}} + \delta J$.

3.4 The Ronen iterative scheme

The Ronen algorithm used to solve the critical eigenvalue problem in the slab is described as follows (see Fig. 3):

1. *Initialize* The algorithm receives the geometry and the cross sections (XS) of the problem as input data. At this stage, the correction factors $\delta D^{(0)}$ are set to zero and the initial pure-diffusion operator is constructed, that is $\mathcal{A}^{(0)} = \mathcal{A}_0$. Initial guesses for the flux $\phi^{(0)}$ and the multiplication factor $k_{\mathrm{eff}}^{(0)}$ are set.
2. *Diffusion solver* A one-dimensional multigroup diffusion solver is executed with the migration operator $\mathcal{A}^{(k)} = \mathcal{A}_0 + \delta A^{(k)}$ to determine new estimates of the flux $\phi^{(k)}$ and of the multiplication factor $k_{\mathrm{eff}}^{(k)}$.

Table 1 Two-group macroscopic cross sections [cm^{-1}] of the homogeneous case [11]

Group g	σ_g	$\sigma_{s,0,g\leftarrow g'}$		χ_g	$\nu\sigma_{f,g}$
1	5.3115×10^{-1}	5.04664×10^{-1}	2.03884×10^{-3}	1	7.15848×10^{-3}
2	1.30058×10^{0}	1.62955×10^{-2}	1.19134×10^{0}	0	1.41284×10^{-1}

Table 2 Reactivity differences as a function of mesh refinement using the Ronen method

dx (cm)	I	k_{ref}	k_{D}	$\Delta\rho_{\mathrm{D}}$ (pcm)	k_{RM}	$\Delta\rho_{\mathrm{RM}}$ (pcm)
0.43	50	0.744307	0.741417	−524	0.740552	−681
0.215	100	0.744391	0.741355	−550	0.743447	−171
0.1075	200	0.744412	0.741339	−557	0.744212	−36
0.07167	300	0.744416	0.741336	−558	0.744356	−11
0.05375	400	0.744417	0.741335	−558	0.744407	−2

3. *Convergence check* Convergence is checked with the relative residuals on the flux and on the multiplication factor between iteration k and $(k-1)$; Ronen iterations are stopped if the relative residuals fall within the input tolerances.
4. *Estimate currents* Both the diffusion current $J_{\mathrm{D}}^{(k)}$ (Eq. 20) and the transport current $J_{\mathrm{tr}}^{(k)}$ (Eq. 19) are calculated using $\phi^{(k)}$ and $k_{\mathrm{eff}}^{(k)}$.
5. *Update correction* The correction factors $\delta D^{(k+1)}$ are obtained using $\delta J^{(k)}$ and Eq. (21) in order to update the migration operator $\mathcal{A}^{(k+1)} = \mathcal{A}_0 + \delta\mathcal{A}^{(k+1)}$ (Eq. 25), and continue with step 2.

4 Results

Two one-dimensional test cases are considered: homogeneous and heterogeneous. The reference solutions are calculated using a Python3 discrete ordinates S_N code with $N = 16$ [18]. The diffusion solutions and the Ronen iterations are produced using original codes in Python3. All tolerances on relative residuals are set to 1E−6 in the iterative solving schemes, and no (over/under)-relaxation is done. The initial diffusion coefficient is set to $D = 1/(3\sigma_{tr}) = 1/(3\sigma)$ since only isotropic scattering is considered in this case. Anisotropic scattering cases are deferred to future studies. Void boundary conditions are used at the outer edges of the core, which are implemented for the diffusion solver in the form of a group-dependent extrapolated distance, i.e., $d_g = 2.13D_g$, see Sect. 3.3.

4.1 Homogeneous case

A homogeneous slab of width $a = 21.5$ cm is considered, with the two-group macroscopic cross sections shown in Table 1.

Table 2 shows the reactivity differences as a function of mesh refinement using standard diffusion (with extrapolated length) and the Ronen method. The reactivity difference is given by $(\Delta\rho = 1/k_{\mathrm{ref}} - 1/k_{\mathrm{D/RM}}) \times 10^5$ pcm, where k_{D} and k_{RM} are the multiplication factors of standard diffusion and of the Ronen method, respectively. The reference k_{ref} value from S_{16} is 0.744417 ($I = 400$).

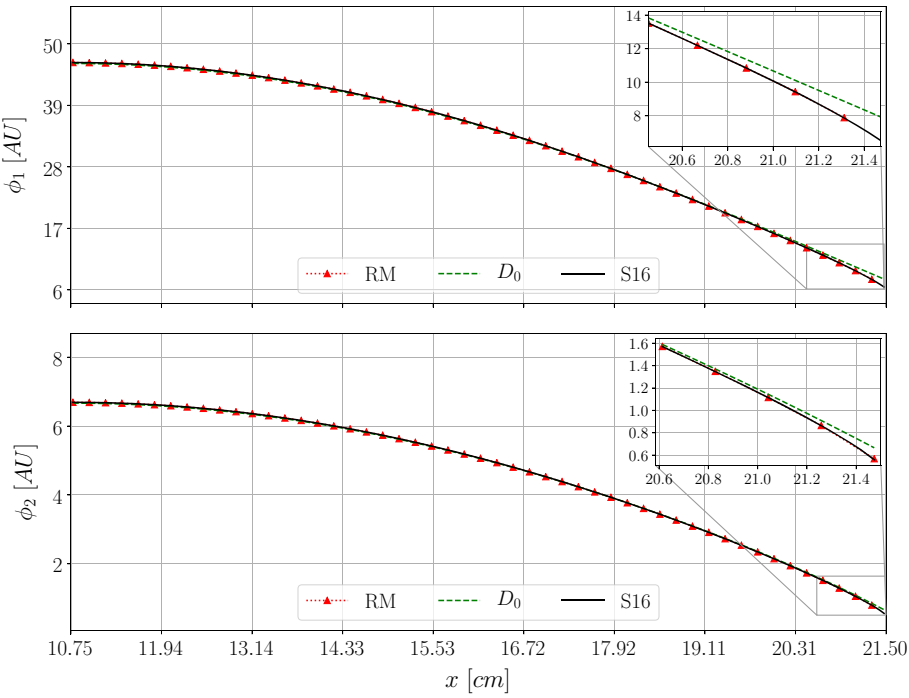

Fig. 4 Comparison of the fluxes as calculated by the reference S_N code, the RM code, and a standard multigroup diffusion without RM correction (D_0). The insets show a zoom-in of the fluxes near the boundary. Results shown here after 250 Ronen iterations

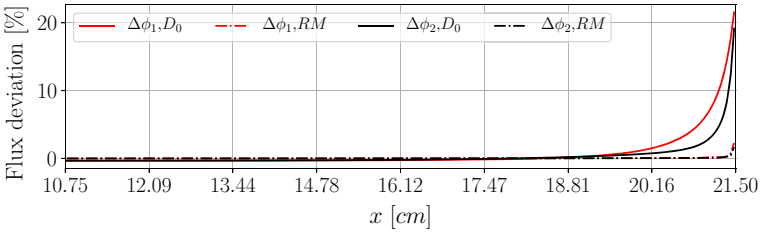

Fig. 5 Deviation of the fluxes with respect to the reference solution after 250 Ronen iterations

A comparison of the fast and thermal fluxes, as calculated by the reference S_N code, the RM code, and the standard multigroup diffusion without RM correction (denoted by D_0), is shown in Fig. 4 for the half slab. The deviations (in [%]) of the RM-corrected flux and of the standard diffusion flux from the reference S_N flux are also shown in Fig. 5. The corresponding Ronen method correction factors δD are shown in Fig. 6.

The deviation from the reference solution is decreased by the Ronen iterations from approximately 20% near the boundary and 1% at the slab center to 2% and 0.01%, respectively.

The RM correction terms (δD) along the slab are shown in Fig. 6. It is possible to observe that the diffusion correction almost vanishes at the slab center and exhibits non-trivial behavior near the boundary. The convergence of the flux (max deviation) and that of the criticality eigenvalue are shown in Fig. 7, where $\epsilon_\phi = \max[\phi^{(k)} - \phi^{(k-1)})/\phi^{(k-1)}]$ and

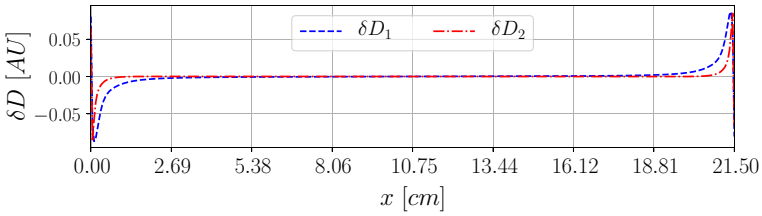

Fig. 6 The Ronen method correction factors (δD). Results shown here after 250 Ronen iterations

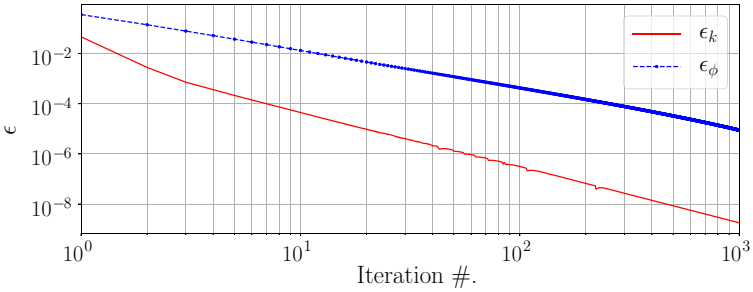

Fig. 7 Convergence of the flux (max deviation) and of the criticality eigenvalue during 1000 Ronen iterations

$\epsilon_k = (k_{\text{eff}}^{(k)} - k_{\text{eff}}^{(k-1)})/k_{\text{eff}}^{(k-1)}$. While the eigenvalue converges within a few iterations, relatively slow convergence is noticed for the flux with higher differences against the reference S_{16} solution near the boundaries. The spatial flux convergence between two successive Ronen iterations is shown in Fig. 8 for the left half slab, according to $\Delta\phi = (\phi^{k-1} - \phi^k)/\phi^{k-1}$ [%]. The spatial flux convergence of the Ronen iterations with respect to the reference solution for the left half slab is shown in Fig. 9 instead.

Notice the change of sign in the flux convergence $\Delta\phi$ in Fig. 8 between the center (negative) and the boundary (positive) of the slab. The initial diffusion solution is smoother than the transport one. Hence, it can be seen in Fig. 4 that the diffusion solution underestimates the peak flux at the center of the slab and overestimates the flux near the boundary. The Ronen iterations "push" the diffusion solution toward the transport one by increasing the flux level at the center of the slab and decreasing the flux level at the boundary. Hence, $\phi^{(k-1)}$ is smaller at the center and higher at the boundary compared to $\phi^{(k)}$. This effect caused by Ronen iterations produces less smooth flux shape with steeper gradients comparing to the diffusion solution.

4.2 Heterogeneous case

The heterogeneous benchmark defines three heterogeneous cores; each is 7 fuel assemblies long and comprised of four different fuel assemblies made of four different materials [24], as shown in Fig. 10. Material properties for each region of the assemblies are given in Table 3. Configuration 1 represents the least heterogeneous core with rather smooth flux gradients. On the contrary, configuration 3 represents the most heterogeneous core with the steepest flux gradients and can serve as a limiting case [24]. Void boundary conditions are imposed on both ends of the core.

Table 4 shows the reactivity differences between standard diffusion (with extrapolated length) and the Ronen method (at increasing number of iterations) with respect to the reference

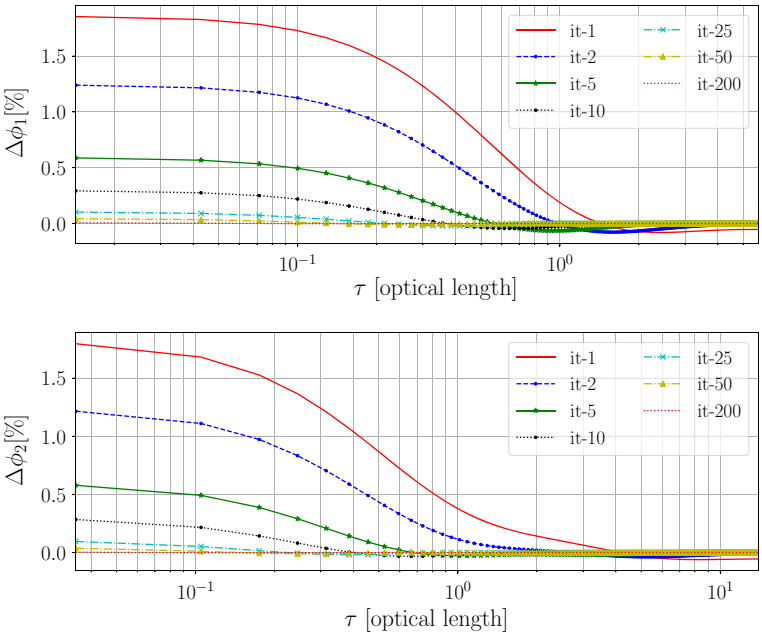

Fig. 8 The spatial flux convergence between two successive Ronen iterations for the left half slab, according to $\Delta\phi = (\phi^{(k-1)} - \phi^{(k)})/\phi^{(k-1)}$ [%]

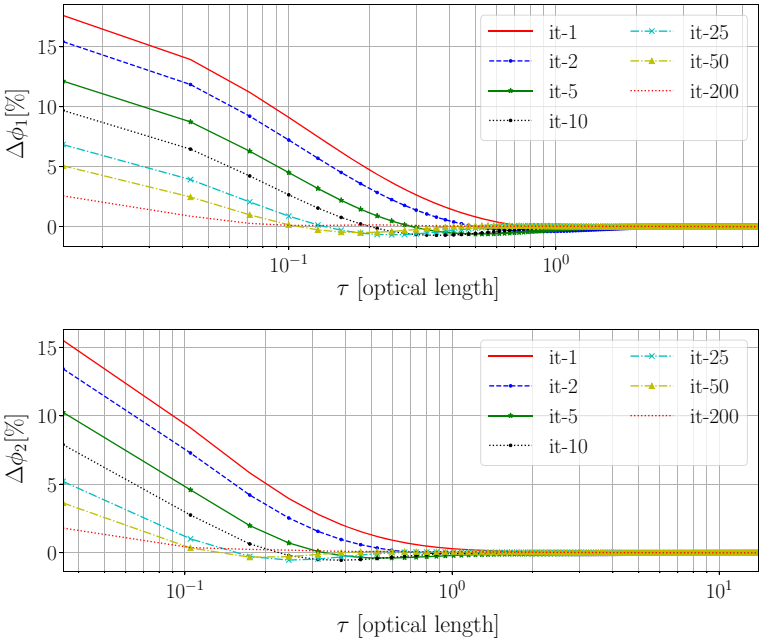

Fig. 9 The spatial flux convergence of the Ronen iterations with respect to the reference S_{16} solution for the left half slab

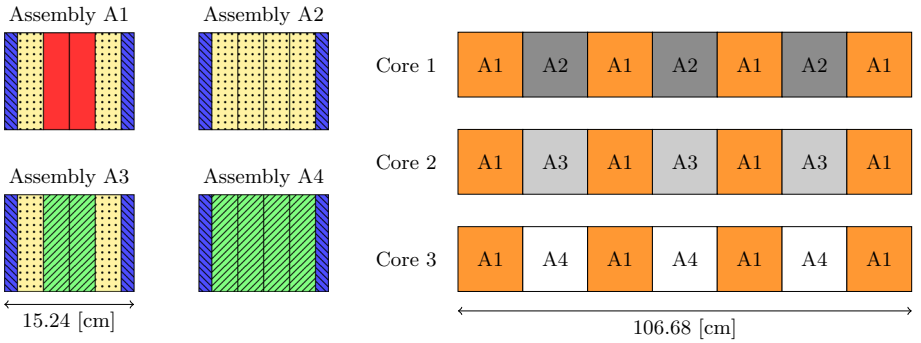

Fig. 10 Schematic illustration of the fuel assemblies and core composition and geometry [24]

Table 3 Two-group macroscopic cross sections [cm^{-1}] used for the heterogeneous case [24]. Colors are in accordance with Fig. 10

Material	σ_1	σ_2	$\nu\sigma_{f,1}$	$\nu\sigma_{f,2}$	$\sigma_{s,1\leftarrow1}$	$\sigma_{s,2\leftarrow1}$	$\sigma_{s,2\leftarrow2}$	x (cm)
Water (blue)	0.1890	1.4633	0.0000	0.0000	0.1507	0.0380	1.4536	1.158
Fuel 1 (red)	0.2263	1.0119	0.0067	0.1241	0.2006	0.0161	0.9355	3.231
Fuel 2 (yellow)	0.2252	0.9915	0.0078	0.1542	0.1995	0.0156	0.9014	3.231
Fuel 3 (green)	0.2173	1.0606	0.0056	0.0187	0.1902	0.0136	0.5733	3.231

Table 4 Reactivity differences as a function of number of iterations using the Ronen method. 728 nodes

Method	Core 1		Core 2		Core 3	
	k_{eff}	$\Delta\rho$ (pcm)	k_{eff}	$\Delta\rho$ (pcm)	k_{eff}	$\Delta\rho$ (pcm)
S_{16}	1.25614	–	1.00094	–	0.79878	–
Diffusion	1.25902	182	0.99325	−773	0.77805	−3335
RM-10	1.25677	40	1.00107	13	0.79824	−85
RM-20	1.25648	22	1.00091	−3	0.79837	−64
RM-50	1.25625	7	1.00076	−18	0.79839	−61
RM-100	1.25618	3	1.00070	−24	0.79838	−62

solution for each of the three core configurations. The standard diffusion solution performs rather well for core 1 with deviation of 182 pcm, but fails for cores 2 and 3 with deviation of 773 and 3335 pcm, respectively. This is explained by the fact that cores 2 and 3 are more heterogeneous compared to core 1. The Ronen method performs better than standard diffusion for all three cores, even after merely 10 iterations. Additional Ronen iterations further improve the estimated multiplication factor until convergence within the prescribed tolerance.

The two-group flux distribution across each core is shown in Fig. 11 for standard diffusion (D_0), Ronen method (RM) and the S_{16} reference solution. RM results are shown for 100 iterations, and the spatial mesh spans 8 nodes in the water and 22 nodes in each fuel element. On a first glance, it is easy to see that standard diffusion fails to produce the steep flux gradients

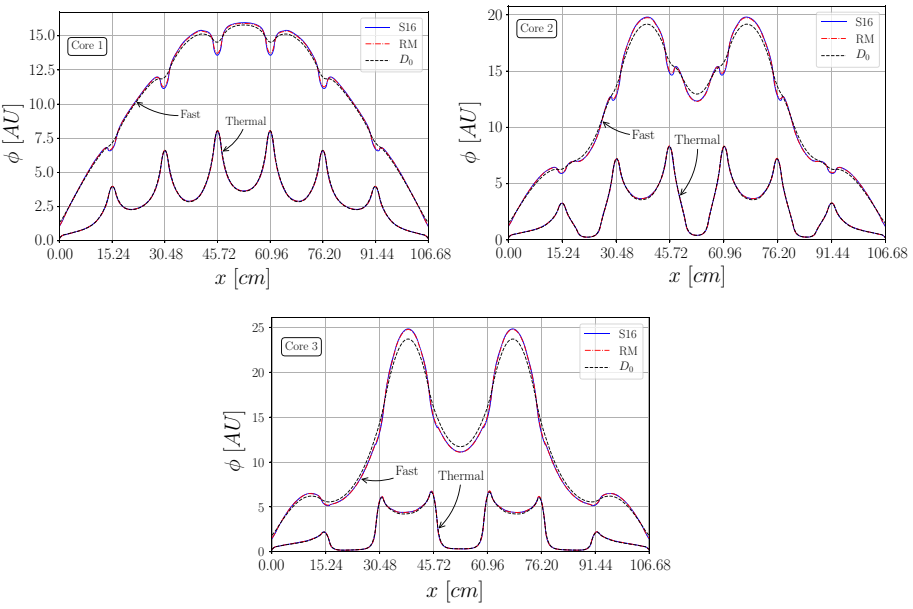

Fig. 11 Fast and thermal flux for each core using standard diffusion (D_0), Ronen method (RM) and S_{16} reference solution. Vertical grid lines are located at assemblies interfaces. RM results are for 100 iterations, and the spatial mesh spans 8 nodes in the water and 22 nodes in each fuel element

across material interfaces, especially between fuel and water. This is more pronounced for the fast flux, where even in core 1 it is not described correctly.

The fast and thermal flux deviation of standard diffusion (D_0) and Ronen method (RM) with respect to S_{16} reference solutions is shown for each core in Fig. 12. The fast flux is poorly reproduced by standard diffusion, with up to $\sim 10\%$ deviations at the inner interfaces and $\sim 20\%$ at the outer boundaries (in agreement with the homogeneous case). Deviations of the thermal flux calculated by diffusion increase from ~ 4 to $\sim 10\%$ as the heterogeneity of the core increases. The deviations of the fast and thermal flux calculated by Ronen method are much smaller, with practically negligible values in the fuel and less than $\sim 2\%$ in the water.

It is illustrative to examine the spatial distribution of the Ronen method correction factors for the heterogeneous case. The behavior of the correction factor (Fig. 13) may seem a bit erratic, but can be explained. In regions where the flux gradients are small, the correction factors tend to vanish and actually produce solutions similar to standard diffusion. However, in regions where the flux gradients are steep, the correction factors do not vanish and play an important role in reproducing the correct flux shape.

5 Conclusions

The Ronen method was first proposed for better estimates of the diffusion coefficient by calculating the current with a higher-order transport operator and a known best-estimate neutron flux. This yielded an iterative scheme leading to new flux distributions solved by a diffusion solver but with additional (spatially) corrected diffusion terms, driving the diffusion solution to that of the integral transport equation.

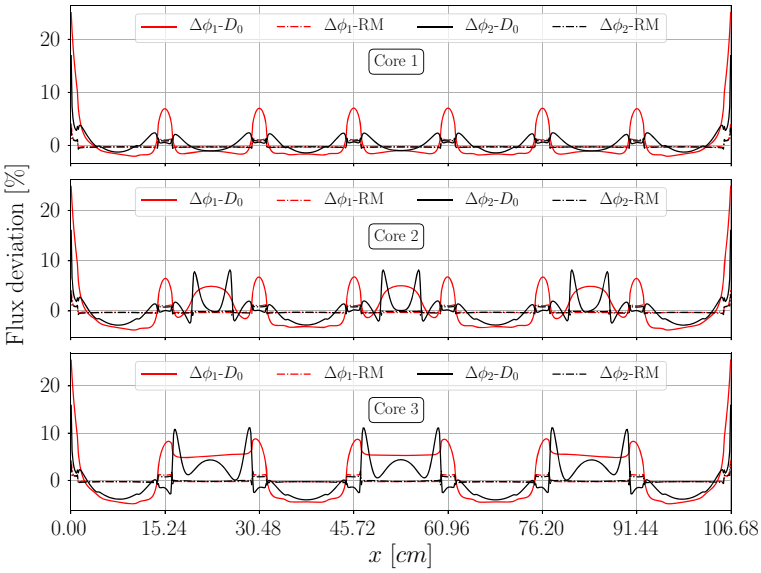

Fig. 12 Fast and thermal flux deviation of standard diffusion (D_0) and Ronen method (RM) with respect to S_{16} reference solutions for each core. Vertical grid lines are located at assemblies interfaces. RM results are for 100 iterations, and the spatial mesh spans 8 nodes in the water and 22 nodes in each fuel element

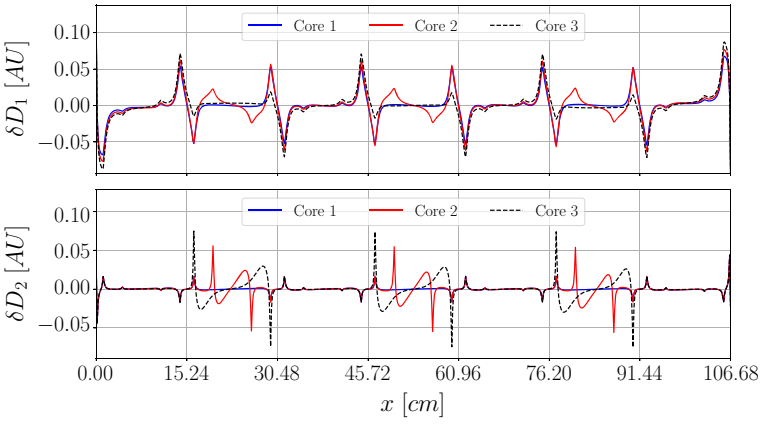

Fig. 13 Behavior of the Ronen method correction factor δD along the core, for the fast and thermal fluxes. Vertical grid lines are located at assemblies interfaces, results are for 100 iterations, and the spatial mesh spans 8 nodes in the water and 22 nodes in each fuel element

The basic relation proposed by Ronen, i.e., Eq. (3), becomes problematic in the regions where the gradient of the flux is small, that is usually where diffusion performs well. Ronen did not elaborate on this issue in his technical note from 2004. Theoretically, both the numerator and the denominator should vanish at the same location since both are accurate expressions for the neutron current with weak flux gradients. We assume that this ratio, considered as a ratio between two quantities which tend to zero at the same location, approaches some constant value since there exist a diffusion coefficient at that location. However, any value would be possible in Fick's law because of the vanishing flux gradient.

Numerically, Tomatis and Dall'Osso chose in 2011 to deal with this potential singularity by using the well-known drift terms, which serve as a *numerical feature*. The (more accurate) surface current J_{tr}, calculated by the integral expression, is written as the sum of the surface current calculated by diffusion, J_{D}, plus a correction δJ. Hence, when the current vanishes, the correction δJ vanishes as well. Moreover, the correction is written as in Eq. (21), avoiding the potential divergence resulting from division by zero.

More accurate results are obtained for the two-group benchmark problem reported in [11], and new results are reported for a heterogeneous benchmark. The performances of the Ronen method, especially for the heterogeneous benchmark (as shown in Figs. 11, 12, 13), strongly indicate that it is inherently suitable to deal with non-homogeneous systems and can naturally adapt to interfaces, where strong gradients of the flux might appear.

In general, slow convergence is observed for the scalar flux with the larger discrepancies, compared to the reference, located on the vacuum boundary and on the material interfaces. Although the method is converging to the reference results provided by a discrete ordinate transport code, the improvement of the convergence rate and the use of coarser meshes are crucial for the advancement of the methodology in practical applications. These topics will be addressed as future developments, as well as higher-order anisotropy.

Acknowledgements The authors express their gratitude to Prof. Yigal Ronen who initiated the idea for this study. R.G. is partially supported by the Israel Ministry of Energy, Contract No. 216-11-008.

References

1. J. Kim, Y. Kim, Development of 3-D HCMFD algorithm for efficient pin-by-pin reactor analysis. Ann. Nuclear Energy **127**, 87–98 (2019)
2. W.R. Martin, Challenges and prospects for whole-core Monte Carlo analysis. Nuclear Eng. Technol. **44**(2), 151–160 (2012)
3. K. Smith, Monte Carlo for practical LWR analysis: what's needed to get to the goal? in *American Nuclear Society Summer Meeting, M&C Division, Computational Roundtable*, Hollywood, FL, June 27, 2011 (2011)
4. R.D. Lawrence, Progress in nodal methods for the solution of the neutron diffusion and transport equations. Prog. Nuclear Energy **17**(3), 271–301 (1986)
5. K.S. Smith, Assembly homogenization techniques for light water reactor analysis. Prog. Nuclear Energy **17**(3), 303–335 (1986)
6. F. Bertrand, N. Marie, G. Prulhière, J. Lecerf, J.M. Seiler, Comparison of the behaviour of two core designs for ASTRID in case of severe accidents. Nuclear Eng. Des. **297**, 327–342 (2016)
7. IAEA, *Best Estimate Safety Analysis for Nuclear Power Plants: Uncertainty Evaluation. Number 52 in Safety Reports Series* (International Atomic Energy Agency, Vienna, 2008)
8. G.I. Bell, S. Glasstone, *Nuclear Reactor Theory* (Van Nostrand Reinhold, New York, 1970)
9. J.M. Pounders, F. Rahnema, On the diffusion coefficients for reactor physics applications. Nuclear Sci. Eng. **163**, 243–262 (2009)
10. P.S. Brantley, E.W. Larsen, The simplified P_3 approximation. Nuclear Sci. Eng. **134**, 1–21 (2000)
11. D. Tomatis, A. Dall'Osso, Application of a numerical transport correction in diffusion calculations, in *International Conference on Mathematics and Computational Methods Applied to Nuclear Science and Engineering (M&C 2011)*, Rio de Janeiro, RJ, Brazil, May 8–12, 2011, 05 (2011)
12. Y. Ronen, Accurate relations between the neutron current densities and the neutron fluxes. Nuclear Sci. Eng. **146**(2), 245–247 (2004)
13. K.S. Smith, Nodal method storage reduction by nonlinear iteration. Trans. Am. Nuclear Soc. **44**, 265–266 (1983)
14. B. Davison, J.B. Sykes, *Neutron Transport Theory* (Oxford University Press, Oxford, 1957)
15. K.M. Case, P.F. Zweifel, *Linear Transport Theory* (Addison-Wesley, Reading, 1967)
16. G.C. Pomraning, *The Equations of Radiation Hydrodynamics* (Pergamon Press, Oxford, 1973)
17. J.J. Duderstadt, W.R. Martin, *Transport Theory* (Wiley, New York, 1979)
18. E.E. Lewis, W.F. Miller, *Computational Methods of Neutron Transport* (Wiley, New York, 1984)

19. M. Abramowitz, I.A. Stegun, *Handbook of Mathematical Functions with Formulas, Graphs, and Mathematical Tables* (Dover, New York, 1964)
20. Y.A. Cengel, M.N. Özişik, Integrals involving Legendre polynomials that arise in the solution of radiation transfer. J. Quant. Spectrosc. Radiat. Transf. **31**(3), 215–219 (1984)
21. J.J. Settle, Some properties of an integral that occurs in problems of radiative transfer. J. Quant. Spectrosc. Radiat. Transf. **52**(2), 195–206 (1994)
22. I.S. Gradshteyn, I.M. Ryzhik, *Table of Integrals, Series, and Products*, 7th edn. (Academic Press, London, 2007)
23. J.R. Lamarsh, *Introduction to Nuclear Reactor Theory* (Addison-Wesley, Reading, 1966)
24. F. Rahnema, E.M. Nichita, Leakage corrected spatial (assembly) homogenization technique. Ann. Nuclear Energy **24**(6), 477–488 (1997)